PCCP

RSC Publishing

PAPER

Modeling charge recombination in dye-sensitized solar cells using first-principles electron dynamics: effects of structural modification†

Cite this: *Phys. Chem. Chem. Phys.*, 2013, **15**, 17187

Wei Ma, Yang Jiao and Sheng Meng*

Received 13th June 2013,
Accepted 16th August 2013

DOI: 10.1039/c3cp52458b

www.rsc.org/pccp

We have performed real-time excited state simulations of electron injection and charge recombination at a dye/semiconductor interface within the framework of time-dependent density functional theory (TDDFT). We found that by inserting a phenyl ring into the organic dye, the charge recombination rate is slowed down by about four times, while the injection rate keeps almost the same. This introduces a drastic increase in the energy conversion efficiency by several folds, in agreement with experimental observations. Quantum simulations thus provide a new way to understand the role of the dye's building blocks and offer new strategies to optimize individual energy transfer steps for improving the efficiency in renewable energy applications.

1. Introduction

As one of the most abundant renewable energy sources, solar energy exceeds the global energy consumption by 4 orders of magnitude.[1–5] Dye-sensitized solar cells (DSC), harvesting incident photons and converting solar energy into electricity have received intensive attention since 1991 due to the low-cost, flexible, environmentally friendly and easy-manufacturing characteristics.[6–10] However, the highest solar-to-electrical energy conversion efficiency for molecular DSC is only 12.3% under AM1.5 irradiation obtained by Grätzel *et al.* in 2011,[11] which is still low for large-scale implementation. Thermal relaxation and charge recombination are two major energy loss processes limiting the overall energy conversion efficiency.[12–14] Electrons in excited states after photo-excitation, if not rapidly injected, easily lose the absorbed photon energy as heat through electron–phonon scattering and subsequent phonon dissipation, thus generating (thermal) loss in efficiency.[15–20] On the other hand, as more and more electrons accumulate in the semiconductor conduction band (CB), the electrons, if not effectively transported to the transparent conductive oxide electrode for electron collection, easily recombine with holes in dyes and in the electrolyte, a dominant process responsible for major energy losses.[21–24] Therefore, improving the injection rate and retarding the recombination process are two effective ways to optimize DSC.

An interesting example towards this goal is illustrated by Haid *et al.* In 2012, Haid and coworkers synthesized a group of donor-π-acceptor (D-π-A) dyes for application in DSC.[25] They found that the insertion of an additional phenyl ring between the acceptor and the π linker has a significant influence on the solar cell's performance: a drastic increase in the energy conversion efficiency (η = 8.21%) was observed, 6.5 times higher than that using sensitizers without the phenyl group (η = 1.24%). Further photophysical measurements attribute this behavior to the significant difference in the electron recombination rate of the two dyes: the insertion of an additional phenyl group in the π-linker slows down the recombination rate by over five times. Preliminary quantum mechanical simulations carried out by these authors seem to suggest the additional phenyl ring induces a significant out-of-plane torsion with respect to the bridging unit after a photoelectron injected to the TiO_2 film, thus breaking down the π-conjugation between the donor and acceptor and blocking the electron back transfer to the sensitizer from the charge separated state.

In general, when and why some small modifications in the dye's atomic structure would lead to a dramatic difference in DSC performance remains unclear and needs to be carefully investigated. For a full understanding of the dye solar cell performance and the roles of its building blocks and the associated structural modifications, the molecular structure, electronic coupling mechanism, and electronic dynamics at the dye–semiconductor interface is of crucial importance. In this regard, quantum mechanical simulations are believed to be most promising and even superior over some elusive experimental investigations, since most experimental tools are not surface-sensitive and unraveling complex interface details at the molecular level experimentally is extremely challenging.

Beijing National Laboratory for Condensed Matter Physics, and Institute of Physics, Chinese Academy of Sciences, 100190 Beijing, China. E-mail: smeng@iphy.ac.cn

† Electronic supplementary information (ESI) available. See DOI: 10.1039/c3cp52458b

This journal is © the Owner Societies 2013

Although the ground state and static properties at the dye/TiO_2 interface have been intensively explored with theory calculations, real time first-principles simulation on critical electron dynamics including photoelectron injection and recombination has been a daunting task. Previous works were mainly based on optimized structural features and ground-state molecular dynamics simulations, and/or with empirical kinetic models and parameters, such as exponential decay of the electron injection rate as a function of the dye length[26,27] and constant electron coupling strength.[28] To give some examples, Prezhdo *et al.* reproduce the injection dynamics of model chromophores with atomistic details using ground state molecular dynamics simulation and time domain non-adiabatic trajectory surface hopping based on ground-state trajectories.[29–32] Abuabara *et al.* successfully investigated the influence of temperature changes on the electron injection at dye/TiO_2 interface using ground-state molecular dynamics, and studied the electron transfer process using an extended Hükel Hamiltonian.[33] Li *et al.* studied electron transfer from perylene derivatives into the anatase TiO_2 (101) surface using density functional theory (DFT) and a Fock matrix partitioning method.[34] Jones *et al.* could rapidly predict the injection rate in DSC by partitioning the system into molecular and semiconductor subsystems and computing the retarded Green's function.[35] However, such theoretical models cannot adequately address the electronic properties in excited states, for instance, excited state potential energy surfaces (PES), which are different from ground state PES, are missing in these simulations. Furthermore, they cannot describe precisely the electronic couplings at the interface, which is subject to molecular details of the dyes and their dynamic binding configurations on TiO_2, thus the time scales obtained therein are questionable. In addition, only a few of these studies have been devoted to investigating charge recombination processes,[36,37] where they suffer from the same problems mentioned above. Therefore, directly viewing electron transfer dynamics, especially for recombination, across the chromophore–semiconductor interface is strongly needed for a better understanding of interface electronic dynamics.

Here we apply the new real time TDDFT approach[38] to simulate electron recombination dynamics at dye/TiO_2 interface based on first-principles. Real-time dynamics within the framework of time-dependent density functional theory (TDDFT) is employed to evolve quantum mechanically the wavefunctions of an excited electron–hole pair at the dye/TiO_2 interface based on the excited state Hamiltonian, to produce real time dynamical characteristics of charge transfer at the interface.[38] Embracing the advantages of this approach, we have successfully simulated the real-time dynamics of electron injection and recombination, and reproduced nicely the experimental findings. We found that model dye N2 (molecular structure shown in Fig. 1a) with an additional phenyl ring in the π-linker has a timescale of 23 ps for electron recombination, four time slower than the dye N1 (Fig. 1a) without a phenyl ring (~6 ps), while the injection rates for both dyes are almost the same (140 fs for N2 and 160 fs for N1). More importantly, our detailed DFT calculations show that electron-injection-induced molecular twisting is questionable, and cannot account for the retarded recombination observed experimentally. Further investigations reveal that the large difference in the recombination rates of N1 and N2 mainly comes from their distinct electron transfer distances.

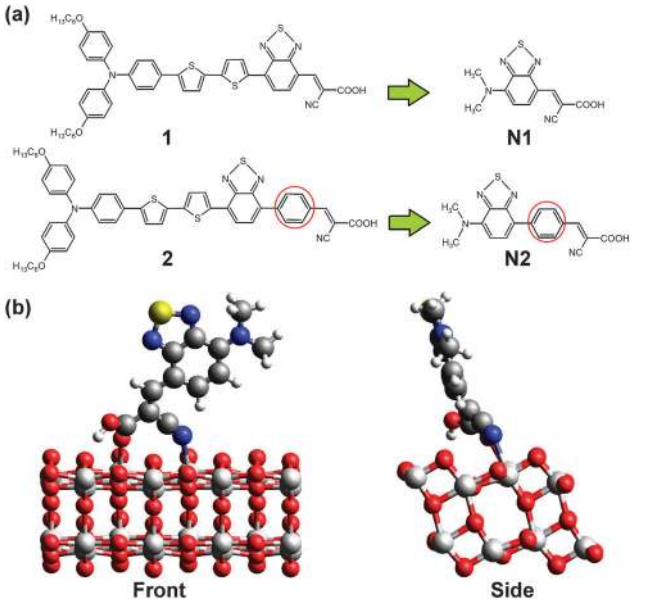

Fig. 1 (a) Chemical structures of dyes 1 and 2, N1 and N2. (b) Front and side view of the simulation cell and the binding configuration of the chromophore on the TiO_2 anatase (101) surface. The chromophore is anchored to the semiconductor *via* the carboxyl group and the cyano group. The slab contains six layers of TiO_2 with periodic boundary conditions in dimensions along the surface plane. Color scheme: Ti – light grey, O – red, C – dark grey, N – blue, S – gold, H – white.

2. Methodology

2.1. Simulation method and models

First-principles density functional theory calculations[39] were carried out with the SIESTA code.[40] The simulation cell contains organic dyes bonded at TiO_2 anatase (101) surface, which is the dominant and thermodynamically stable facet,[41] *via* the carboxyl group and the cyano group (Fig. 1b). Two simple donor-π-acceptor (D-π-A) sensitizers N1 and N2, which are simplified models of dye 1 and 2, respectively, in Haid *et al.*'s work,[25] are adopted as sample dyes. These two sensitizers comprise a dimethylamino donor (D) and a benzothiadiazole (BTDA)-substituted cyanoacrylic acid as the acceptor and anchoring group (A). Dye N1 contains the BTDA group directly adjacent to the cyanoacrylic acid anchoring group, while dye N2 contains an additional phenyl ring between BTDA and the cyanoacrylic anchor (Fig. 1a). Solvent molecules are not considered in our model, since they usually participate only in weak interactions such as van der Waals interactions and their influence is subject to future investigations. Periodic boundary conditions are applied to replicate the simulation cell in all three dimensions and create an array of TiO_2 slabs. A sufficient large vacuum layer (at least 10 Å) is added to the simulation cell in the direction perpendicular to the surface to ensure that no interactions occur between each slab.

 This journal is © the Owner Societies 2013

The ground state electronic and atomic structures of dyes/TiO_2 are computed using the pseudopotentials of the Troullier–Martins type[42] to model the atomic cores, the Perdew–Burke–Ernzerhof (PBE) exchange–correlation functional,[43] and a local basis set of double-ζ polarized (DZP) orbitals (19 numerical atomic orbitals for Ti including semicore 3s and 3p states;[44] 13 orbitals for C, N, O and S; 5 orbitals for H). An auxiliary real space grid equivalent to a plain wave cutoff of 150 Ry is used for the calculation of the electrostatic (Hartree) term. Geometries are optimized until forces on non-fixed atoms are below 0.005 eV $Å^{-1}$. A large simulation cell, 10.24 × 15.14 × 30.00 Å, containing four-layer TiO_2 slab and organic chromophores, corresponding to a surface coverage of one dye per 155 $Å^2$ or 1.07 μmol m^{-2} is used. The Brillouin zone was sampled at the Γ point.

The optical absorption spectra were calculated based on linear response time-dependent DFT (TDDFT) using the LC-PBE and CAM-B3LYP functionals and 6-31G(d) basis set, as implemented in Gaussian 09 program. The structural optimization of N1, N2, dye 1, and dye 2 was performed using both SIESTA with PBE functional and DZP basis set described above and the Gaussian package with CAM-B3LYP functional and 6-31G(d) basis set.

2.2. Electronic dynamics simulation

In our simulations of electron injection and electron–hole recombination processes, the evolution of both electrons and ions in real time is monitored after photo excitation. The time-dependent Kohn–Sham equations of electrons and the Newtonian motion of ions are solved simultaneously, with ionic forces along the classical trajectory evaluated through the Ehrenfest theorem. The coupled ion–electron equations are expressed as,

$$M_J \frac{\mathrm{d}^2 \boldsymbol{R}_J^{\mathrm{cl}}(t)}{\mathrm{d}t^2} = -\nabla_{\boldsymbol{R}_J^{\mathrm{cl}}} \left[V_{\mathrm{ext}}^J\left(\boldsymbol{R}_J^{\mathrm{cl}}, t\right) - \int \frac{Z_J \rho(\boldsymbol{r}, t)}{\left|\boldsymbol{R}_J^{\mathrm{cl}} - \boldsymbol{r}\right|} \mathrm{d}\boldsymbol{r} + \sum_{I \neq J} \frac{Z_J Z_I}{\left|\boldsymbol{R}_J^{\mathrm{cl}} - \boldsymbol{R}_I^{\mathrm{cl}}\right|} \right] \tag{1}$$

$$\begin{aligned} i\hbar \frac{\partial \phi_j(\boldsymbol{r}, t)}{\partial t} = & \left[-\frac{\hbar^2}{2m} \nabla_r^2 + \nu_{\mathrm{ext}}(\boldsymbol{r}, t) - \int \frac{\rho(\boldsymbol{r}', t)}{|\boldsymbol{r} - \boldsymbol{r}'|} \mathrm{d}\boldsymbol{r}' \right. \\ & \left. - \sum_I \frac{Z_I}{\left|\boldsymbol{r} - \boldsymbol{R}_I^{\mathrm{cl}}\right|} + \nu_{\mathrm{xc}}[\rho](\boldsymbol{r}, t) \right] \phi_j(\boldsymbol{r}, t) \end{aligned} \tag{2}$$

where $\boldsymbol{r}_j$ and $\boldsymbol{R}_J$ are the positions of electrons and Jth ion, respectively; m and M_J denote the mass of electrons and of the Jth ion; Z_J denotes the ionic charge; ν_{ext} is the external potential and ν_{xc} is the exchange–correlation potential that depends only on the corresponding density ρ. To quantitatively analyze the charge transfer and electron–hole separation process, we use the integral of excited electron (hole) density projected onto the TiO_2 orbitals, as a function of time after photoexcitation, with χ defined as,

$$\chi = \int \mathrm{d}\boldsymbol{r} |\tilde{\psi}(\boldsymbol{r})|^2, \quad \tilde{\psi}(\boldsymbol{r}) = \sum_{j \in \mathrm{TiO_2}} c_j \phi_j(\boldsymbol{r}) \tag{3}$$

where c_j are the coefficients of the atomic basis states ϕ_j in the Kohn–Sham orbital $\psi_{\mathrm{KS}}(\boldsymbol{r})$ of interest (either the excited electron or the hole).

$$\psi_{\mathrm{KS}}(\boldsymbol{r}) = \sum_j c_j \phi_j(\boldsymbol{r}) \tag{4}$$

The electron density is updated self-consistently during the real time propagation of Kohn–Sham wave functions with a time step of 0.02419 fs. The initial velocity of ions is assigned according to the equilibrium Boltzmann–Maxwell distribution at a given temperature of 350 K. Within this scheme, the total energy is well conserved to within 10^{-4} eV fs^{-1}, which is proven to be accurate enough to produce negligible differences in the energy levels evolution and electron–ion dynamics. Better performance can be obtained if a more stringent criterion for each step is chosen. Although the standard functionals do not treat charge-transfer excitation well, a long-range corrected functional should be more accurate for the excitation energies. In our dynamics simulation, the exact excitation energy is not the focus but the energy alignment and the timescales. We have shown in a previous work that the energy level alignment is correctly reproduced by DFT with PBE functional.[45]

3. Results and discussion

3.1. Electronic structure

We first illustrate how the model dyes, N1 and N2, bind onto the anatase TiO_2 (101) surface, the dominant facet in DSC devices. We have chosen various initial adsorption configurations of dye N1 and N2 onto the substrate, and optimized the binding structure for each of them. We found that the optimized structure shown in Fig. 1b has the lowest total energy, indicating it is the preferred binding configuration. Both N1 and N2 dyes bind to the surface through its carboxyl group and the cyano group. In the initial configuration of the dye–TiO_2 system, the hydrogen of the –COOH anchoring group stays on the dye, but after optimization it is found to transfer to the substrate predominantly in a protonated state. As a result, the most stable tridentate anchoring mode is adopted with adsorption energy of 1.55 eV for N1 and 1.43 eV for N2, respectively. This conclusion is in good agreement with previous calculations.[45]

Then we calculate the alignment of electronic levels of the dye–TiO_2 system. Fig. 2a and b show the projected density of states (PDOS) of dyes N1 and N2, where the energy is measured against the vacuum energy level. The calculated electronic structure agrees well with the required electronic structure for DSCs, namely the lowest unoccupied molecular orbital (LUMO) of the sensitizer lies above the conduction band minimum (CBM) of the semiconductor TiO_2 substrate (about −4.0 eV *vs.* vacuum), meanwhile the highest occupied molecular orbital (HOMO) lies in the gap between the conduction band and the valence band (VB). The calculated HOMO and LUMO energies were −5.57 and −3.86 eV for N1 and −5.22 and −3.69 eV for N2, respectively. Larger N2 chromophore shows a 0.18 eV smaller band gap as compared to N1, consistent with the general concept

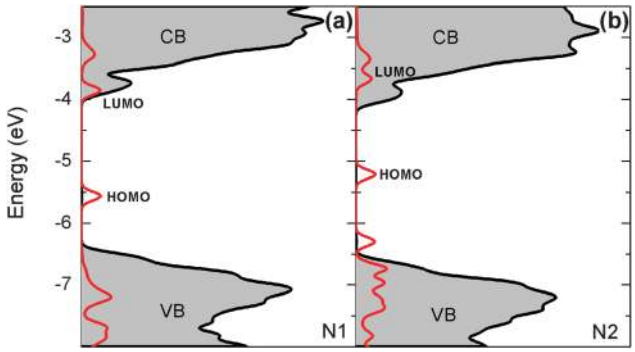

Fig. 2 Projected density of states (PDOS) of dye N1 (a) and dye N2 (b).

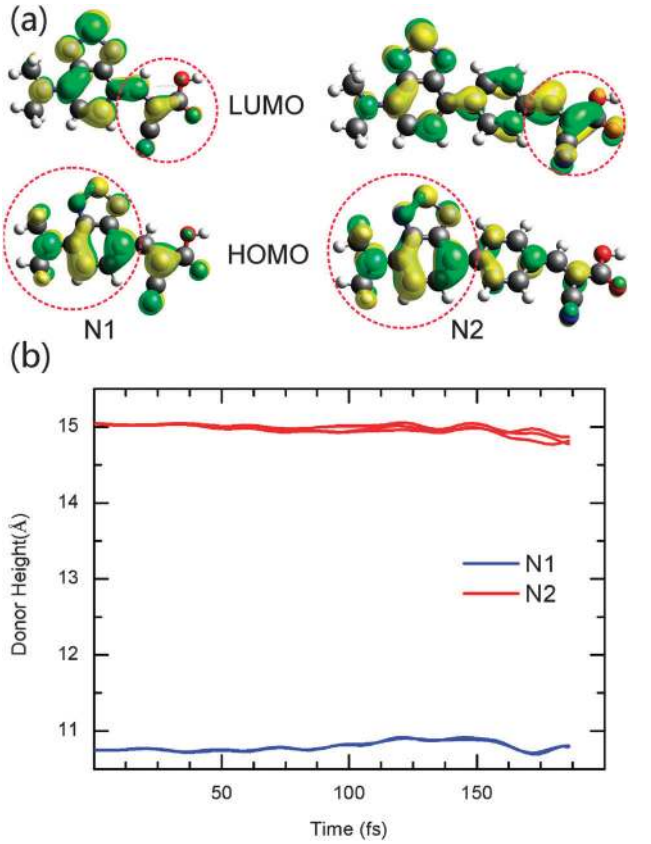

Fig. 3 (a) Wave functions of HOMO and LUMO frontier orbitals of dyes N1 and N2. (b) Evolution of the vertical distance from the donor N atom to the Ti linked with the O of the anchoring carboxyl after photo-excitation. The blue (red) lines show the evolution of the donor height from several MD trajectories for N1 (N2).

that larger molecules have a smaller gap. While ground-state DFT may underestimate the band gap of molecules and materials, the relative difference in energy alignment is still meaningful. In addition, we also calculate photo absorption of these dyes by TDDFT (see Fig. S1, ESI†). The position of the first absorption peak is correlated with the ground-state HOMO–LUMO gap, but with the electron–hole interactions and the screening effects included. The maximum photo absorption wavelength of 432 nm (2.87 eV) for N1 and 455 nm (2.73 eV) for N2 exhibited a similar trend as in DFT band gaps. Interestingly, the insertion of a phenyl group between BDTA and the cyanoacrylic group in the experimental dye 1 introduces a blue shift in the absorption peak (from 579 to 515 nm),[25] due to a significant reduction in the electron delocalization. Our calculations reproduce nicely this trend measured in the experiment: the wavelength for the maximum absorption is 581 nm for dye 1 and 559 nm for dye 2. This demonstrates that quantum simulations perform well in describing the absorption property of organic dyes.

From Fig. 2a and b, one finds that the HOMO and LUMO levels of N2 are obviously up-shifted as compared to N1, leading to a larger driving force ΔG^0_{inj} for electron injection (0.02 eV for N1 and 0.33 eV for N2), which is defined as the energy difference between LUMO and the TiO_2 CBM ($\Delta G^0_{inj} = E_{LUMO} - E_{CBM}$). This allows an efficient electron injection from the sensitizers into the TiO_2 electrode. The higher HOMO and LUMO levels of N2 are considered the result of the lower positive surface dipole moment, thus resulting in a larger band level difference ΔG^0_{inj}. It is demonstrated that ΔG^0_{inj} linearly decreases with the surface dipole moment induced by dye adsorption.[43] Orbital population analysis was performed by calculating the intergral of wave function distributions on the TiO_2 substrate of the LUMO orbital of the chromophore, which reveals that the electrons in the LUMO of N2 have 57.8% located in the substrate while in N1 they are only 8%, meaning the LUMO of N2 is a mixing state with contributions from both the molecule and TiO_2. Therefore N2 has a strong coupling with the TiO_2 semiconductor, resulting in the up-shift of the LUMO.

We further calculate the wave function of the frontier orbitals of dyes N1 and N2 in order to penetrate into the electronic properties of these two dyes (Fig. 3a). The HOMO and LUMO orbitals of dye N1 are slightly delocalized, leading to better conjugation between the donor and the acceptor group, while in dye N2, the HOMO orbital is more localized in the donor moiety and the LUMO orbital is more localized in the acceptor moiety. The HOMO and LUMO orbitals of both dyes are sufficiently overlapped between the donor and the acceptor group to ensure a fast charge transfer transition. Therefore, excitation from the HOMO to the LUMO could lead to efficient electron transfer from the donor to TiO_2 *via* the anchoring cyanoacrylic acid group.

3.2. Injection process in DSC

The influence of small structural changes on the electron injection efficiency is further investigated based on TDDFT. Fig. 4 shows the fractions of electrons injected into the TiO_2 semiconductor as a function of time after photo-excitation, illustrating an ultra fast electron injection process at the organic dye/TiO_2 interface. At time t = 0, one electron is promoted from the HOMO to the LUMO of the organic dyes, representing the first excited state that a pair of electron and hole is generated upon photo absorption. Electronic state diagonalization is performed at this first step after the occupation switch. Then we let the coupled electron–ion system evolve in real time. The initial ionic temperature is set to 350 K. As in Fig. 4, excited electrons are completely injected into the CB of the TiO_2 substrate within a time scale of 162 fs for N1 and 146 fs

 This journal is © the Owner Societies 2013

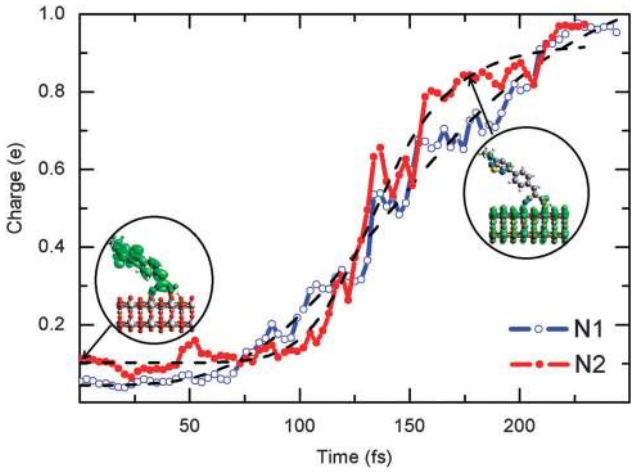

Fig. 4 Fraction of electrons injected to the TiO_2 semiconductor substrate as a function of time after photo-excitation at the organic dye/TiO_2 interface. Dashed lines are a result fitted by a constant delay followed by an exponential decaying dynamics. The two insets are the electron density of N2 upon photoexcitation (t = 0 fs) and after charge separation (t = 175 fs).

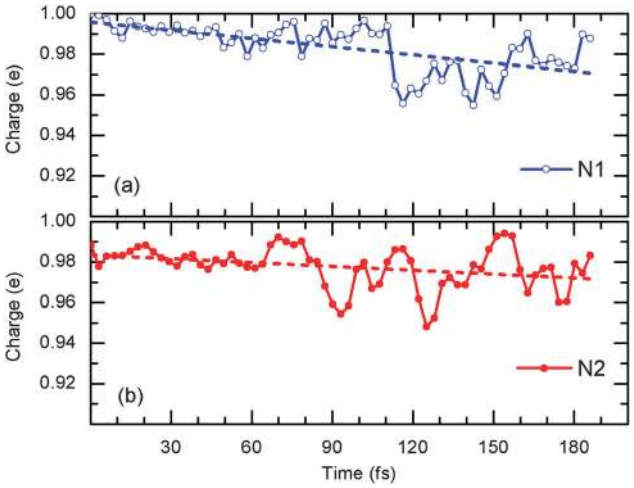

Fig. 5 Fraction of electrons transferred from the TiO_2 semiconductor substrate to the organic dyes N1 (a) and N2 (b) after excitation at the organic dye–TiO_2 interface. Dashed lines are results fitted by a linear decaying dynamics.

for N2, while the holes keep stable and confined within the dye molecules. Here the lifetime of the injection process is estimated by the time when 63.2% electrons are transferred from the sensitizer into the TiO_2 electrode.

3.3. Recombination process in DSC

We also explore the influence of the additional inserted phenyl ring on the charge recombination process of the two dyes. The electron–hole recombination simulation starts with an electronic excited state that corresponds to the excitation of an electron from HOMO of the dye to the CB of the TiO_2, which is a good approximation for representing the initial charge separated state for back transfer and recombination. Different kinds of initial excitation states are sampled, which correspond to excitations from HOMO of the dye to different energy states of TiO_2 CB (H → L + 1, H → L + 2, H → L + 7, H → L + 9 for N1; H → L + 2, H → L + 3, H → L + 7 for N2). All these final states are low energy states of TiO_2 CB and do not represent substantial physical differences. Other excitations do not converge easily in our simulations; to save computer time we focus on these trajectories only. The electron distribution on the semiconductor substrate after excitation is monitored using first-principles electronic dynamics simulation based on TDDFT. Immediately after promoting an electron to the CB of TiO_2, the electrons have a dominant distribution in the CB of the TiO_2. The energy difference between the CB of the TiO_2 and the HOMO of the dye drives electron transfer from TiO_2 to the sensitizer. Fig. 5 shows the average results of different trajectories of the recombination process in N1 and N2. The recombination rates of both dyes exhibit a good linear decaying dynamics and the longer molecule clearly shows slower decaying behavior. The time-scales of the recombination process, 6 ps for N1 and 23 ps for N2, are obtained by extending the linear curve to the intersection where all electrons are back transferred to the dye. This is in agreement with experimental observations that the recombination rate is 5 times slower in dye 2 (60 μs) sensitized devices than that for dye 1 (12 μs), measured by nanosecond laser photocatalysis.[25] Here the contrast between dye 1 and 2 is more important than the real values in timescales, due to the drastic complexity in real devices including differences in molecular sizes, presence of solvents, variations in bonding geometries, *etc*.

By contrast, we note that the time-domain surface hopping approach based on ground state trajectories produces too fast recombination for N1 (146 fs) and failed to account for the finite lifetime for electron recombination for N2/TiO_2 interface (see Fig. S2, ESI†). The fast recombination dynamics with a time scale comparable to the electron injection (146 fs *versus* 162 fs) for N1 would suggest that a very low electron injection efficiency in the experiment and the corresponding solar cells cannot work. The results produced by surface hopping are thus at variance with the experiment.

3.4. Theoretical analysis of charge transfer dynamics in DSC

To fully understand the different behaviors of N1 and N2 dyes produced by first-principles dynamics simulation, we present a more transparent, semiclassical analysis of the charge transfer dynamics. The lifetime of an electron transfer process is determined by the electron transfer rate, $\tau = \frac{1}{k_{ET}}$. According to the Marcus theory,[46] semiclassical treatments have provided the following simple expressions for the rate of nonadiabatic electron transfer between two centers held at a fixed distance and orientation:

$$k_{ET} = \sqrt{\frac{\pi}{\hbar^2 \lambda k_B T}} |V|^2 \exp\left(\frac{-\left(-\Delta G^0 + \lambda\right)^2}{4\lambda k_B T}\right) \quad (5)$$

In eqn (3), λ corresponds to the reorganization energy, ΔG^0 is the driving force for the reaction, T is the absolute temperature for the system. V is the electron coupling strength between the

donor and acceptor, which is exponentially dependent on the electron transfer distance with an attenuation factor β,[47]

$$V^2 \propto \exp(-\beta r). \quad (6)$$

In an injection process, an electron transfers from the LUMO orbital of the dye to the TiO_2 CB. Thus the transfer distance of the injection process is between the cyanoacrylic acid anchoring group and the TiO_2 surface, which is almost identical for N1 ($\sim$2.31 Å) and N2 ($\sim$2.29 Å), shown in Fig. S3 (ESI†). The driving force is 0.02 eV for N1 and 0.33 eV for N2, resulting in big differences in the activation energy for electron injection $\Delta G^* = (-\Delta G^0 + \lambda)^2/4\lambda$ (0.20 eV for N1 and 0.02 eV for N2) thus leading to different injection rates. Therefore, we attribute the slightly faster injection rate for N2 to its smaller activation energy.[48] Since the injection process in DSC is very fast, this tiny difference in injection rates hardly affects their energy conversion efficiency.

In the recombination process, an electron transfers back from the TiO_2 CB to the HOMO orbital of the dye. The transfer distance is defined by the distance between the donor moiety of the dye to the interface, which is $\sim$11 Å for N1 and $\sim$15 Å for N2, respectively, taking the position of a potential minimum in the dye donor region as the center of the donor group (Fig. S3, ESI†). The evolution of the donor height after photo-excitation is shown in Fig. 3b, obtained from several molecular dynamics trajectories on N1–TiO_2 and N2–TiO_2 systems. It is demonstrated that the recombination distance of N2 is obviously larger than N1 throughout the whole back electron transfer process. The driving forces for the recombination processes are 1.68 eV for N1 and 1.19 eV for N2. The estimations of the driving forces, reorganization energies, charge transfer distances and rates for the injection and recombination dynamics are given in Table 1. The reorganization energy λ is assumed to be the same for both injection and recombination, which can be obtained from DFT calculations on the molecules in solution.[49] The attenuation factor β is estimated from the empirical values in the donor–linker–acceptor system as in a previous work.[47] The injection rate for N1 estimated from this semi-empirical method is identical to our TDDFT simulation result ($\sim$160 fs), while for N2 it shows much discrepancy. The latter is attributed to too small activation energy (ΔG^*) for N2–TiO_2 and the absence of dynamic contributions. The estimated recombination rates for N1 and N2 are 11 and 42 ps, respectively. Two times larger than those from our TDDFT simulations, but the ratio of N1 and N2 is consistent with the TDDFT results, which state N2 has a recombination dynamics four times slower. We note that the difference in driving forces ΔG^0_{rec} has only a weak influence on the difference in recombination rates, and the four times difference in the recombination rate mainly comes from their distinct electron transfer distances. If the two systems have identical electron transfer distances, the recombination rates of the two dyes would be similar and the larger dye even has a faster recombination dynamics.

It was previously reported that the phenyl ring in dye 2 has an additional out-of-plane torsion of $\sim$30° after electron injection (from 18° (neutral form) to 48° (cationic form)), breaking down the π-conjugation between the donor and acceptor, and thus slowing down recombination processes. We prudently optimized the equilibrium structure of the four dyes (dye 1, 2 and N1, N2, see Fig. S4 and Table S1, ESI†), with varying starting geometries where the dihedral angle θ between the BTDA unit and the adjacent phenyl ring range from 0 to 90°. The optimized dye structures have no changes in the dihedral angle between their respective neutral and cationic forms. Dye 1 and N1 prefer to be completely planar with $\theta \approx 1°$, and dye 2 has a 33° dihedral angle in both neutral and cationic forms, while dye N2 has an angle $\theta \approx 20°$. We did not find that electron injection would introduce an additional twist in dye 2, though this dye indeed has a non-planar geometry. Whether this non-planar geometry imposes a significant constraint on electron dynamics is debatable and out of focus of the present work, the similar injection timescales for N1 and N2 seem to indicate that the torsion may not dramatically modify the interface electron dynamics.

We emphasize that the insertion of the phenyl ring between BTDA and the anchoring group increases the back electron transfer distance, thus retarding the recombination process while maintaining an effective injection, leading to a significant improvement in solar cell efficiency. We expect that this strategy is generally applicable to various types of dyes and can be further optimized for a particular group of dyes to achieve a good balance between other competing factors such as dye coverage and photostability of the devices.

Table 1 Estimation of driving forces ΔG^0, reorganization energies λ, activation energies ΔG^*, attenuation factor β, charge transfer distances r and rates k^{-1} for electron injection and charge recombination

Dye	ΔG^0_{inj} /eV	ΔG^0_{rec} /eV	λ^a /eV	$\Delta G_{inj}{}^{*b}$ /eV	$\Delta G_{rec}{}^{*b}$ /eV	r_{inj} /Å	r_{rec} /Å	β /Å^{-1}	$k_{inj}{}^{-1}$ /fs	$k_{rec}{}^{-1}$ /ps
N1	0.02	1.68	0.85	0.20	0.20	2.31	10.75	0.5	166	11
N2	0.33	1.19	0.56	0.02	0.18	2.29	15.05	0.5	2	42

[a] The reorganization energy λ is assumed to be the same for both injection and recombination. [b] Activation energy $\Delta G^* = (-\Delta G^0 + \lambda)^2/4\lambda$.

4. Conclusions

We have applied quantum simulations based on DFT and TDDFT to investigate the crucial effects of structural modification on the electron injection and charge recombination process. By the insertion of an additional phenyl ring close to the anchoring group, the electron–hole recombination rate is slowed down by about four times (23 ps *vs.* 6 ps). Through meticulous structure optimization and analysis, our results confirmed that the charge transfer distance dependence is the main factor for this significant difference in the recombination lifetime. In contrast, both the two dyes exhibit an ultrafast photoelectron injection at a time scale of $\sim$150 fs.

The perfect consistency with the experiment illustrates that first-principles quantum mechanical simulation is a promising and accurate way dealing with electronic interaction and dynamics

 This journal is © the Owner Societies 2013

at the molecule–semiconductor interface at the nanoscale. Interface electronic dynamics is essential in many applications, such as catalysis, sensors and energy conversion. Dynamic simulations provide a direct evidence concerning the stability, reaction pathway, spectroscopic data and decaying lifetimes that can be directly verified in the experiment. In addition, it exhibits a priority in nanoscale systems because experiment tools are usually not surface sensitive and performing an experiment at the nanoscale is extremely challenging. We believe that quantum mechanical simulation will continue to play an indispensable role in the course of interface science research for renewable energy.

Acknowledgements

We are grateful to Drs Gang Lu and Zi Li for assistance with the trajectory surface hopping method. The work is supported by NSFC (grants 11074287 and 11222431), MOST (2012CB921403), and the Hundred-talent program of CAS.

References

1 J. J. Conti, P. D. Holtberg, J. A. Beamon, A. M. Schaal, J. C. Ayoub and J. T. Turnure, *Annual Energy Outlook 2011*, U.S. Energy information Administration, Washington, DC, 2011.
2 M. Z. Jacobson and M. A. Delucchi, *Sci. Am.*, 2009, **301**, 58–65.
3 D. Wöhrle and D. Meissner, *Adv. Mater.*, 1991, **3**, 129–138.
4 K. Zweibel, J. Mason and V. Fthenakis, *Sci. Am.*, 2008, **298**, 64–73.
5 R. István, S. Vaidyanathan, K. Masaru and V. K. Prashant, *J. Am. Chem. Soc.*, 2006, **128**, 2385–2393.
6 B. O'Regan and M. Gratzel, *Nature*, 1991, **353**, 737–740.
7 G. H. Guai, Q. L. Song, C. X. Guo, Z. S. Lu, T. Chen, C. M. Ng and C. M. Li, *Sol. Energy*, 2012, **86**, 2041–2048.
8 B. E. Hardin, E. T. Hoke, P. B. Armstrong, J.-H. Yum, P. Comte, T. Torres, J. M. J. Frechet, M. K. Nazeeruddin, M. Gratzel and M. D. McGehee, *Nat. Photonics*, 2009, **3**, 406–411.
9 P. V. Kamat, *J. Phys. Chem. C*, 2008, **112**, 18737–18753.
10 L. M. Peter, *Phys. Chem. Chem. Phys.*, 2007, **9**, 2630–2642.
11 A. Yella, H.-W. Lee, H. N. Tsao, C. Yi, A. K. Chandiran, M. K. Nazeeruddin, E. W.-G. Diau, C.-Y. Yeh, S. M. Zakeeruddin and M. Grätzel, *Science*, 2011, **334**, 629–634.
12 A. J. Nozik, *Phys. E.*, 2002, **14**, 115–120.
13 M. S. Iván and B. Juan, *J. Phys. Chem. Lett.*, 2010, **20**, 3046–3052.
14 L. M. Peter, *J. Phys. Chem. Lett.*, 2011, **2**, 1861–1867.
15 B. S. Justin, N. Thomas and B. A. Parkinson, *Science*, 2010, **330**, 63–66.
16 P. T. Landsberg, H. Nussbaumer and G. Willeke, *J. Appl. Phys.*, 1993, **74**, 1451–1452.
17 S. Kolodinski, J. H. Werner, T. Wittchen and H. J. Queisser, *Appl. Phys. Lett.*, 1993, **63**, 2405–2407.
18 A. M. William, J. W. Kenrick, A. T. Brooke, J. N. David, S. A. Eray and X. Y. Zhu, *Science*, 2010, **328**, 1543–1547.
19 D. S. Boudreaux, F. Williams and A. J. Nozik, *J. Appl. Phys.*, 1980, **51**, 2158–2163.
20 R. T. Ross and A. J. Nozik, *J. Appl. Phys.*, 1982, **53**, 3813–3818.
21 I. n. Mora-Seró, S. Giménez, F. Fabregat-Santiago, R. Gómez, Q. Shen, T. Toyoda and J. Bisquert, *Acc. Chem. Res.*, 2009, **42**, 1848–1857.
22 L. M. Peter, *Phys. Chem. Chem. Phys.*, 2007, **9**, 2630–2642.
23 S. Manzhos, H. Segawa and K. Yamashita, *Chem. Phys. Lett.*, 2011, **504**, 230–235.
24 W. Mou, S. Ohmura, F. Shimojo and A. Nakano, *Appl. Phys. Lett.*, 2012, **100**, 203306.
25 S. Haid, M. Marszalek, A. Mishra, M. Wielopolski, J. Teuscher, J.-E. Moser, R. Humphry-Baker, S. M. Zakeeruddin, M. Grätzel and P. Bäuerle, *Adv. Funct. Mater.*, 2012, **22**, 1291–1302.
26 W. J. E. Beek and R. A. J. Janssen, *J. Mater. Chem.*, 2004, **14**, 2795–2800.
27 C.-W. Chang, L. Luo, C.-K. Chou, C.-F. Lo, C.-Y. Lin, C.-S. Hung, Y.-P. Lee and E. W.-G. Diau, *J. Phys. Chem. C*, 2009, **113**, 11524–11531.
28 S. Manzhos, H. Segawa and K. Yamashita, *Chem. Phys. Lett.*, 2011, **501**, 580–586.
29 W. R. Duncan and O. V. Prezhdo, *Annu. Rev. Phys. Chem.*, 2007, **58**, 143–184.
30 W. R. Duncan, C. F. Craig and O. V. Prezhdo, *J. Am. Chem. Soc.*, 2007, **129**, 8528–8543.
31 W. R. Duncan and O. V. Prezhdo, *J. Phys. Chem. B*, 2005, **109**, 17998–18002.
32 W. R. Duncan, W. M. Stier and O. V. Prezhdo, *J. Am. Chem. Soc.*, 2005, **127**, 7941–7951.
33 S. G. Abuabara, L. G. C. Rego and V. S. Batista, *J. Am. Chem. Soc.*, 2005, **127**, 18234–18242.
34 J. R. Li, M. Nilsing, I. Kondov, H. B. Wang, P. Persson, S. Lunell and M. Thoss, *J. Phys. Chem. C*, 2008, **112**, 12326–12337.
35 D. R. Jones and A. Troisi, *Phys. Chem. Chem. Phys.*, 2010, **12**, 4625–4634.
36 K. H. Deuk and O. V. Prezhdo, *J. Phys.: Condens. Matter*, 2012, **24**, 363201.
37 Z. Li, X. Zhang and G. Lu, *J. Phys. Chem. C*, 2012, **116**, 9845–9851.
38 S. Meng and E. Kaxiras, *J. Chem. Phys.*, 2008, **129**, 054110.
39 W. Kohn and L. J. Sham, *Phys. Rev.*, 1965, **140**, A1133–A1138.
40 J. M. Soler, E. Artacho, J. D. Dale, A. Garcia, J. Junquera, P. Ordejon and D. Sanchez-Portal, *J. Phys.: Condens. Matter*, 2002, **14**, 2745–2779.
41 M. Lazzeri, A. Vittadini and A. Selloni, *Phys. Rev. B: Condens. Matter*, 2001, **63**, 155409.
42 N. Troullier and J. L. Martins, *Phys. Rev. B: Condens. Matter*, 1991, **43**, 1993–2006.
43 E. Artacho, E. Angalada, O. Dieguez, J. D. Gale, J. Junquera, R. M. Martin, P. Ordejon, J. M. Pruneda, D. Sanchez-Portal

and J. M. Soler, *J. Phys.: Condens. Matter*, 2008, **20**, 064208.
44 J. Junquera, M. Zimmer, P. Ordejón and P. Ghosez, *Phys. Rev. B: Condens. Matter*, 2003, **67**, 155327.
45 Y. Jiao, F. Zhang, M. Graetzel and S. Meng, *Adv. Funct. Mater.*, 2013, **23**, 424–429.
46 T. J. Meade, H. B. Gray and J. R. Winkler, *J. Am. Chem. Soc.*, 1989, **111**, 4353–4356.
47 J. Wiberg, T. Marinado, D. P. Hagberg, L. Sun, A. Hagfeldt and B. Albinsson, *J. Phys. Chem. B*, 2010, **114**, 14358–14363.
48 M. J. DeVries, M. J. Pellin and J. T. Hupp, *Langmuir*, 2010, **26**, 9082–9087.
49 T. Marinado, D. P. Hagberg, M. Hedlund, T. Edvinsson, E. M. J. Johansson, G. Boschloo, H. Rensmo, T. Brinck, L. Sun and A. Hagfeldt, *Phys. Chem. Chem. Phys.*, 2009, **11**, 133–141.

 This journal is © the Owner Societies 2013